Geochemistry, Geophysics, Geosystems

RESEARCH ARTICLE
10.1029/2020GC009177

This article is a companion to Harmon et al. (2020), https://doi.org/10.1029/2020GC009174.

Key Points:
- Marine magnetotelluric data are used to better understand the lithosphere-asthenosphere boundary at the central Middle Atlantic Ridge
- A dynamic lithosphere-asthenosphere boundary is observed and compatible with geodynamic modeling
- Partial melt fraction, 1–7%, is estimated based on the inverted resistivity models and consistent with previous studies

Correspondence to:
S. Wang,
s4wang@ucsd.edu

Citation:
Wang, S., Constable, S., Rychert, C. A., & Harmon, N. (2020). A Lithosphere-Asthenosphere Boundary and Partial Melt Estimated Using Marine Magnetotelluric Data at the Central Middle Atlantic Ridge. *Geochemistry, Geophysics, Geosystems*, *21*, e2020GC009177. https://doi.org/10.1029/2020GC009177

Received 12 MAY 2020
Accepted 17 AUG 2020
Accepted article online 20 AUG 2020

Author Contributions:
Data curation: Shunguo Wang, Steven Constable
Formal analysis: Shunguo Wang, Steven Constable
Project administration: Steven Constable, Catherine A. Rychert, Nicholas Harmon
Validation: Catherine A. Rychert, Nicholas Harmon
Writing - original draft: Shunguo Wang, Steven Constable, Catherine A. Rychert, Nicholas Harmon
Writing – review & editing: Shunguo Wang, Steven Constable, Catherine A. Rychert, Nicholas Harmon

A Lithosphere-Asthenosphere Boundary and Partial Melt Estimated Using Marine Magnetotelluric Data at the Central Middle Atlantic Ridge

Shunguo Wang[1], Steven Constable[1], Catherine A. Rychert[2], and Nicholas Harmon[2]

[1]Scripps Institution of Oceanography, University of California San Diego, La Jolla, CA, USA, [2]Ocean and Earth Science, National Oceanography Centre Southampton, University of Southampton, Waterfront Campus, Southampton, UK

Abstract The differential motion between the lithosphere and the asthenosphere is aseismic, so the magnetotelluric (MT) method plays an important role in studying the depth and nature of the lithosphere-asthenosphere boundary (LAB). In March 2016, we deployed 39 marine MT instruments across the Middle Atlantic Ridge (MAR), 2,000 km away from the African coast, to study the evolution of the LAB with ages out to 45 million years (My). The MT acquisition time was limited to about 60 days by battery life. After analyzing dimensionality and coast effects for the MT data, determinant data were inverted for two-dimensional resistivity models along two profiles north and south of the Chain Fracture Zone (CFZ). The imaged thickness of the lithospheric lid (>100 Ωm) ranges from 20 to 80 km, generally thickening with age. In the north of CFZ, punctuated low-resistivity anomalies (<1 Ωm), likely associated with potential partial melts, occur along its base. In the south of CFZ, the base of the resistive lid is demarcated by a low-resistivity channel (<1 Ωm) most likely fed by deeper melts. Sensitivity analyses and structural recovery tests indicate the robustness of these features. Resistivity models are in good agreement with results of seismic data. These results imply that partial melt is persistent over geologic timescales and that the LAB is dynamic features fed by upward percolation of mantle melt. The melt fraction is about 1–7% based on the resistivity, temperature, pressure, and hydrous basalt models, which is consistent with petrophysical observations.

Plain Language Summary The magnetotelluric (MT) method, using natural electromagnetic (EM) fields variations caused by lighting/solar wind, is used to image the depth variation of the lithosphere-asthenosphere boundary (LAB) out to 45 million years (My) at the Middle Atlantic Ridge (MAR). Young oceanic lithosphere is considered geologically simple compared with the continental lithosphere. In March 2016, we deployed 39 MT instruments at the seafloor of the MAR for about 60 days. The deployment was along two profiles (L1 and L2). We processed and analyzed the MT data, and then we inverted the data for electrical resistivity models. The robustness of the resistivity models was tested by various methods. The resistivity model along the L1 shows the depth of the LAB dips from 20 to 80 km as the lithosphere ages from 0 to 45 My. The resistivity model along the L2 shows a low-resistivity channel, which demarcates the base of lithosphere. Other geophysical methods, such as seismic surface-wave tomography and receiver function, agree with the MT results. Our models imply that the partial melt is persistent over geological timescales and the LAB can only be represented by a dynamic model. Melt fracture is estimated as 1–7% using the resistivity and available petrophysical models.

1. Introduction

The lithosphere, which makes up the tectonic plates, is defined as a mechanical layer that translates coherently over a weaker asthenosphere. The lithosphere-asthenosphere boundary (LAB) coincides with the top of the decoupling zone marked by an increase in strain rate (Eaton et al., 2009). Despite the importance of the LAB in plate tectonics, its detection remains elusive. For instance, it is not necessarily illuminated by seismicity, as is the case for convergent, divergent, and transform boundaries. Different proxies are used to demarcate the LAB, depending upon the nature of available observations. From a geodynamic perspective, the LAB can be defined as a transition layer at the base of the thermal boundary layer that separates the conductive lid above from the convective adiabatic mantle below (McKenzie, 1967; Parker & Oldenburg, 1973; Parsons & Sclater, 1977; Stein & Stein, 1992). This depth frequently occurs around

1,250–1,300°C, near the melting point of the mantle rocks, and therefore, an individual isotherm is sometimes used as a proxy for the LAB (Poudjom Djomani et al., 2001). From a seismic perspective, the decrease in *S* wave velocity with depth beneath a high-velocity lid is often associated with the LAB (Rychert et al., 2018b). Sometimes, a change in seismic anisotropy in the upper mantle is used to define the LAB (Burgos et al., 2014; Gaherty & Jordan, 1995; Kawakatsu et al., 2009; Lin et al., 2016; Maggi et al., 2006; Rychert & Harmon, 2017). From the electrical perspective, since the cooler solid lithosphere should be electrically resistive, whereas the hotter viscous asthenosphere should be more conductive, the boundary between a high-resistivity layer above a low-resistivity asthenosphere has been interpreted as the LAB (Eaton et al., 2009). From a petrophysical point of view, there may also be a chemical boundary associated with the LAB, with a dry, chemically depleted peridotite in the lithosphere in comparison to a hydrated, fertile peridotite beneath (Jordan, 1981).

A better understanding of the transition from the rigid lithospheric plate to the weaker mantle beneath has implications for the driving forces of plate tectonics and mantle dynamics. The oceanic lithosphere is an ideal place to study the plate; a thermal plate is predicted to increase in thickness with age, with a gradual transition at its base. A host of scattered wave studies have reported sharp discontinuities in the depth range predicted for the LAB although not necessarily monotonically increasing with age, suggesting that another mechanism besides temperature is required to explain the LAB (Rychert et al., 2018a, 2018b; Tharimena et al., 2017). A compositional plate might be uniformly thick, ~60 km, with sharp base determined by the depth of melting beneath the mid-ocean ridge (Gaherty & Jordan, 1995). Melt in the asthenosphere could also sharpen the LAB transition. Melt is also predicted to decrease the viscosity of the mantle (Hirth & Kohlstedt, 1995), and its presence would therefore define the LAB (Rychert et al., 2005, 2007). The melt itself may be concentrated beneath the plate, decreasing gradually over tens of kilometers in depth, which would best explain a host of observations from scattered waves (Rychert & Shearer, 2009). Alternatively, it has been suggested that melt is concentrated in an ~10 km-thick LAB decoupling channel (Mehouachi & Singh, 2018).

The marine magnetotelluric (MT) method has become important in the understanding of the interior structures of Earth, such as hot spots (Baba, Chen, et al., 2017; Nolasco et al., 1998; Tada et al., 2016), the LAB (Evans et al., 1999, 2005; Key et al., 2013), subduction zones (Matsuno et al., 2010; Naif et al., 2013; Worzewski et al., 2011), and the other Earth dynamics involving melts and hydration (Johansen et al., 2019; Naif et al., 2015, 2016). MT studies proposed that the LAB lies at 150 to 260 km depth beneath the continents and at 20 to >70 km depth beneath the oceans, respectively (Baba et al., 2006; Baba, Tada, et al., 2017; Evans et al., 1999, 2005; Jones et al., 2010; Key et al., 2013; Sarafian et al., 2015). Therefore, the MT method could delineate the depth of the LAB, the melt and hydration in the upper mantle, and, importantly, depth dependence of these properties with age.

The Middle Atlantic Ridge (MAR), being oceanic lithosphere, has a simpler history than the continents. The oceanic plates allow us to study tectonic history starting at the birthplace of a plate, and by studying 0–45 million years (My) of seafloor at the relatively slow spreading ridge, the age-depth variability should generate a large signal. The character of the lithosphere and asthenosphere at the slow spreading MAR (40 mm/year full spreading) (Sinha et al., 1997) is predicted to be much different from the faster spreading East Pacific Rise (EPR) (150 mm/year full spreading), where many of the previous studies have been carried out (Evans et al., 2005; Filloux, 1980; Key et al., 2013; Lizarralde et al., 1995). Also, the slower spreading allows us to study a greater age progression while maintaining good lateral resolution within a reasonable array length.

Our MT measurements at the central MAR are used to capture age variations of the LAB across the Chain Fracture Zone (CFZ), which suggests overall thickening lithosphere with age, but also including perturbation in some regions. We verify our resistivity models against surface wave tomography and receiver function analysis. Partial melts may explain the low-resistivity features, <1 Ωm, in the resistivity models, and we estimate the melt fraction required by the anomalies based on the petrophysical observations and simulations. The resolved dynamic LAB provides a better understanding of the LAB.

2. Marine MT Method

After Cox et al. (1964) made the first measurements of time variations of the seafloor electric and magnetic fields, the marine MT method started to be used to further the understanding of Earth's interior. The source

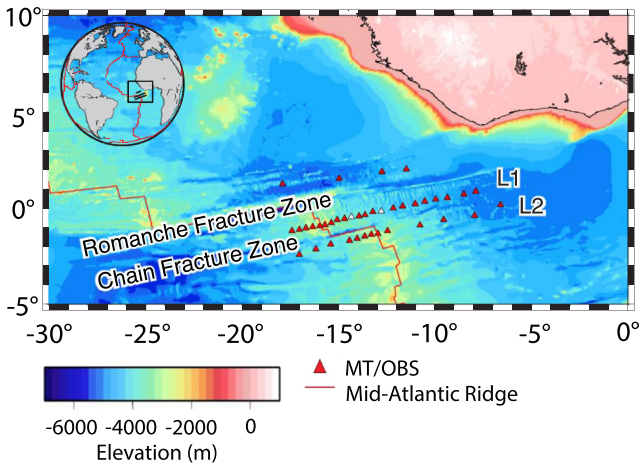

Figure 1. MT instruments and ocean-bottom seismometer (OBS) deployment across the middle Atlantic ridge (MAR). Red triangles are MT stations, white ones lost data. The positions of the Romanche fracture zone (RFZ) and the chain fracture zone (CFZ) are visible. Two profiles, L1 and L2, are in 2-D geometry. Inset map: location of the study area (black box) on a global map. Color represents the elevation at the research area.

fields for MT sounding are temporal variations of Earth's magnetic field, which induce currents and associated electric fields in the conductive parts of the crust and mantle. The magnetic field variation can be caused by lighting, solar wind, and other natural activities.

Although Earth is three-dimensional (3-D), a two-dimensional (2-D) assumption is often used in geophysical surveys, and in many cases the structures of Earth can be simplified in 2-D. This assumption can reduce cost for both data collection and interpretation and at the same time provide necessary information to answer important scientific questions. The 2-D assumption allows us to decompose MT data into a transverse electrical (TE) mode, with electric current flowing approximately along the strike direction, and a transverse magnetic (TM) mode, where current flows in a plane perpendicular to the strike direction (such as the ridge direction).

The simultaneous time series of EM fields can be transformed into frequency domain data; the induced electric fields (E_x, E_y) and the magnetizing fields (H_x, H_y) are related through the frequency-dependent impedance tensor $\boldsymbol{Z}$ given as

$$\begin{bmatrix} E_x \\ E_y \end{bmatrix} = \begin{bmatrix} Z_{xx} & Z_{xy} \\ Z_{yx} & Z_{yy} \end{bmatrix} \begin{bmatrix} H_x \\ H_y \end{bmatrix}, \tag{1}$$

where a Cartesian coordinate system is used in which x represents strike direction, y profile direction, and z depth. Determinant impedance of MT data (Berdichevsky et al., 1980; Pedersen & Engels, 2005) is defined as

$$Z_{det} = \sqrt{Z_{xx}Z_{yy} - Z_{xy}Z_{yx}}. \tag{2}$$

In 2-D media, apparent resistivities ($\rho_{xy/yx/det}$) and phases ($\phi_{xy/yx/det}$) of the TE mode, the TM mode, and the determinant mode can be defined from the Z_{xy}, Z_{yx}, and Z_{det}, respectively, as

$$\rho_{xy/yx/det} = \frac{1}{\mu\omega}\left|Z_{xy/yx/det}\right|^2, \tag{3}$$

$$\phi_{xy/yx/det} = \tan^{-1}\left(\mathrm{Im}\left(Z_{xy/yx/det}\right)/\mathrm{Re}\left(Z_{xy/yx/det}\right)\right), \tag{4}$$

where ω is angular frequency and μ is permeability. Z_{xy} and Z_{yx} are off-diagonal components of the impedance tensor $\boldsymbol{Z}$, and Z_{det} the determinant of the impedance tensor $\boldsymbol{Z}$. Due to the convergence advantage of using logarithmic apparent resistivity and linear phase data in inversion (Wheelock et al., 2015), these scaling are often used to invert resistivity models rather than linear impedance. Determinant data are rotation-free, so that they can be used to suppress 3-D effects and malfunctions of recording compasses (Pedersen & Engels, 2005; Wang et al., 2020). As a synthetic study of a "Hawaiian" plume shown, the 2-D determinant inversion has potentials to resolve the position of the plume and the geometry of the plume head, but both TE and TM-mode inversions failed due to the difficulty of TE- and TM-mode decomposition (Wang et al., 2020).

3. Marine MT Data

The CFZ at the MAR is a 300 km-long transform fault (Figure 1). The Passive Imaging of the Lithosphere Asthenosphere Boundary (PI-LAB) experiment was carried out by international collaboration from different institutions to investigate the LAB at the slow spreading Middle Atlantic Ridge using a range of sensitivities and resolutions in one location (Agius et al., 2018; Harmon et al., 2018; Mehouachi & Singh, 2018; Rychert et al., 2019). We codeployed 39 ocean-bottom MT instruments and 39 Ocean Bottom Seismometer (OBS) instruments at the same time (Figure 1). MT instruments only recorded the first 73 to 101 days of data

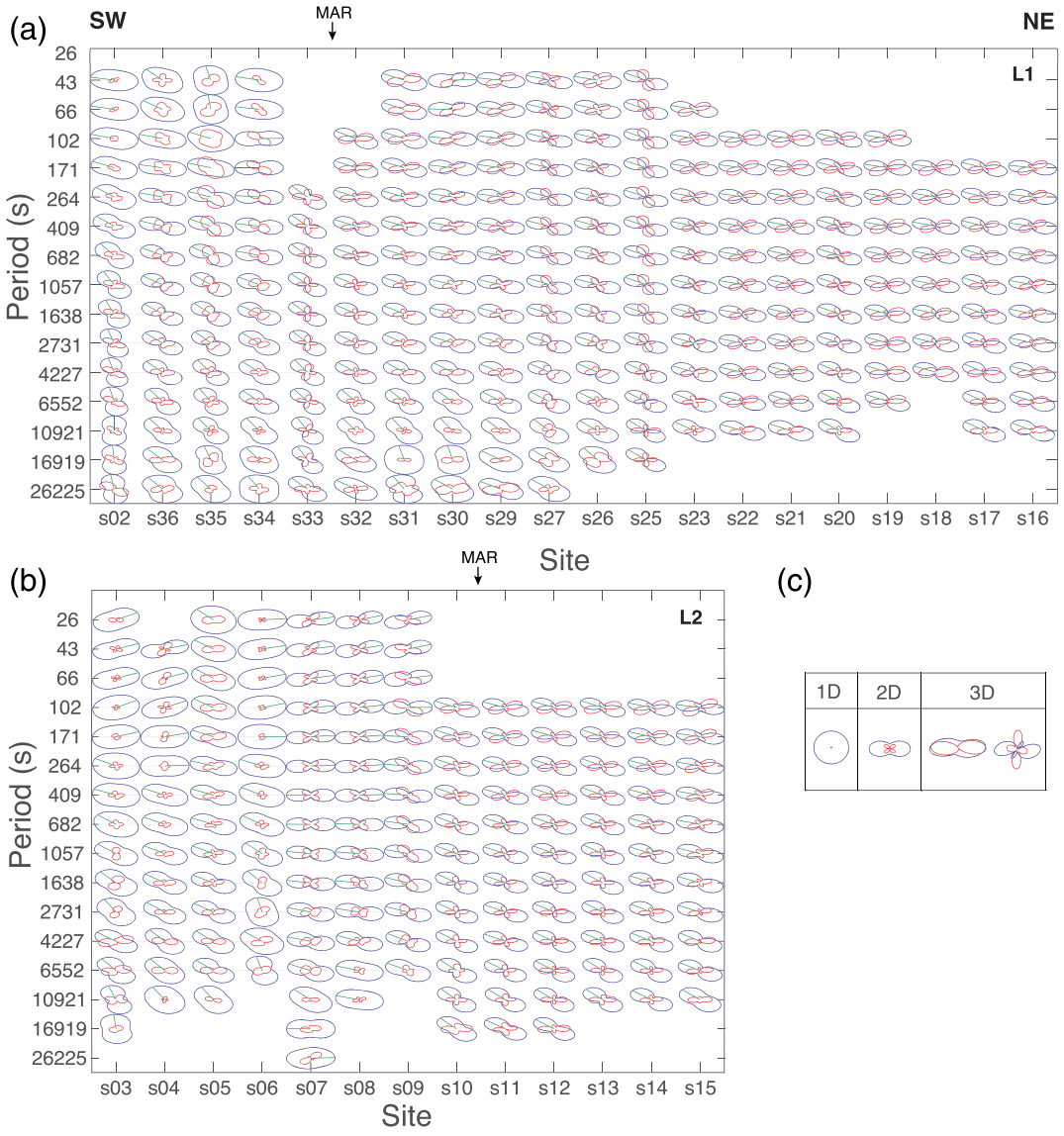

Figure 2. Impedance polar diagrams of MT data. (a) Along Profile L1, (b) along Profile L2, and (c) for different dimensionality of the data. The absolute values of the impedances off-diagonal component (blue lines) and diagonal component (red lines) are plotted as a function of the rotation angle. Ridge direction is perpendicular to the profile direction.

due to a limited battery life, even though they were deployed for 1 year to take the advantage of the seismic recovery cruise.

The sample rate was 62.5 Hz for the MT instruments, and instrument heading, pitch, and roll were recorded using external compasses, estimated to be accurate to 2° (Myer et al., 2012). The data were processed using a multivariate errors-in-variables approach (Egbert, 1997) in groups of four to six sites. Only one site (Site 28) did not produce a reasonable MT response, and one site (24) was lost (white triangles in Figure 1). The periods selected were between 26 and 26,225 s based on data quality and lack of strong 3-D distortion for both profiles (Figure 2); impedance polar diagrams of the selected data show almost parallel orientation due to the similar geology at the different sides of the GFZ, which indicates that there is a preferred orientation for the two profiles. The two profiles show similar preferred orientation since the two lines are perpendicular to the strike of the ridge and are centered on the ridge segments, which have similar structure, but are displaced by the CFZ in between.

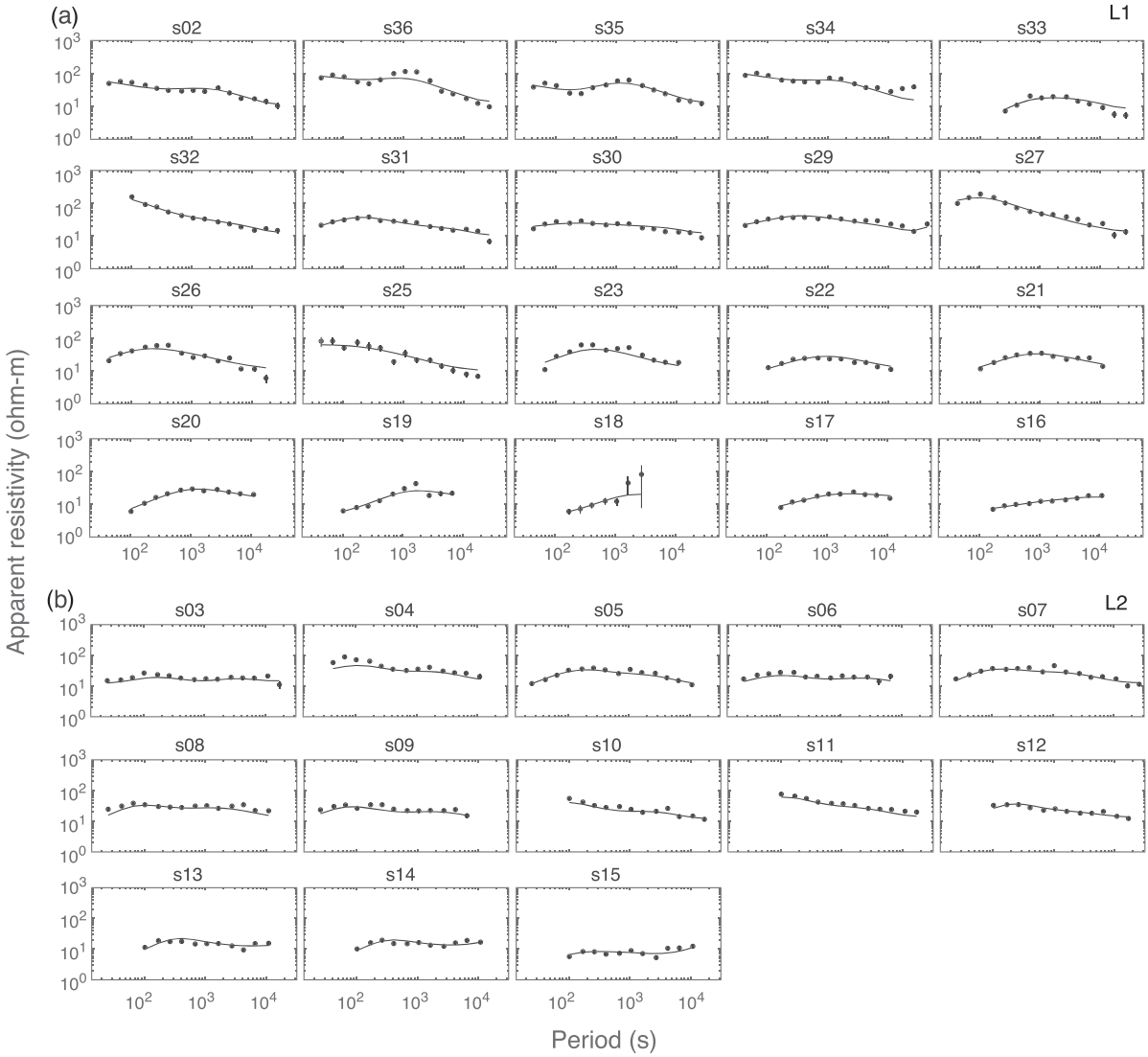

Figure 3. Observed MT data (black dots) are compared to the MT responses of the preferred resistivity models shown in Figure 4 (black lines). (a) Fits along L1. The root mean squared error (RMS) of the inversion is 1.65 with respect to a 10% error floor. (b) Fits along L2. The RMS of the inversion is 1.85 with respect to a 10% error floor. Small error bars are covered by the data dots.

4. Results

4.1. Isotropic Inversion

Coastlines are an extreme case of bathymetry, and in 2-D the classic ocean-side coast effect is associated with lowered TM-mode resistivities as a consequence of electric currents being interrupted by the coastline and TE-mode resistivities, which can have cusps and extreme phase shifts associated with coast-parallel currents that are absent on the landward side (Constable et al., 2009; Key & Constable, 2011; Worzewski et al., 2012). However, there is evidence of another type of coast effect from the nearby 3-D African coastline exhibited as TM-mode negative phases (Wang, Constable, Reyes-Ortega, & Rychert, 2019). Therefore, we modified the 2-D MARE2DEM inversion code (Key, 2016) to invert the determinant apparent resistivities rather than TE- and TM-mode data (Berdichevsky et al., 1980; Pedersen & Engels, 2005), a method which has been shown to produce reasonable 2-D models in the presence of 3-D structures (Pedersen & Engels, 2005; Ranganayaki, 1984; Wang et al., 2020). In contrast to determinant inversion, the TE- and TM-mode inversions of the MAR data set do not converge to a reasonable misfit. Ideally, we would need to carry out 3-D

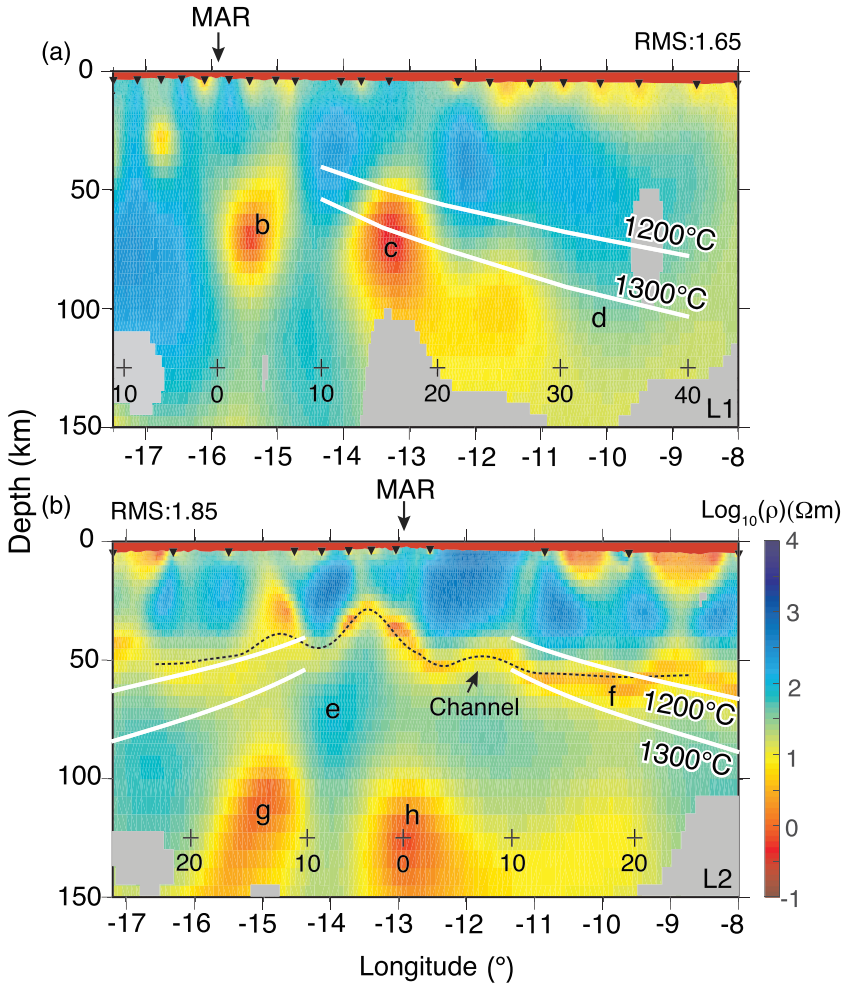

Figure 4. Resistivity models (a) along Profile L1 and (b) along Profile L2. Seafloor ages (in My) are marked as crosses. Letters b, c, and f indicate conductive anomalies for which we have the most confidence, and d and e indicate resistive anomalies. Triangles represent MT instruments. Jacobian percentiles lower than 65% are masked as gray regions. White lines represent isotherms of 1,200°C and 1,300°C for a half-space cooling model (Heinson & Constable, 1992).

inversion of the data. However, this would require inclusion of the entire Atlantic coastline (Wang, Constable, Reyes-Ortega, & Rychert, 2019), as well as detailed local bathymetry, which is beyond the ability of currently publicly available 3-D inversion codes. Also, synthetic studies showed that 2-D determinant inversion can overcome 3-D effect in the marine environment (Wang et al., 2020). Thus, 2-D determinant inversion is an optimal choice in this study.

A 2,000 km distant 2-D coastline and detailed 2-D bathymetry of the study area were included in the models, but the phase data were removed from inversions because when TE- and TM-mode phases have the opposite sign, as is the case here, the determinant phases can be very small. The initial resistivity models used for inversion have 35,375 and 33,743 elements for Profiles L1 and L2, respectively. The initial model for the inversions is a half-space model with a resistivity of 10 Ωm. The horizontal regularization penalty is five times more than the vertical one, which can reduce potential artifacts caused by smoothing in vertical direction. We carried out the inversion using two steps to prevent overfitting and guarantee a smooth model rather than a rough model. The first step is to invert the data until the misfit does not reduce, using a low target root mean square error (RMS) misfit 1. The second step is to repeat the inversion with a new target RMS misfit, which is ~10% higher than the best RMS misfit obtained from the first step. In the second

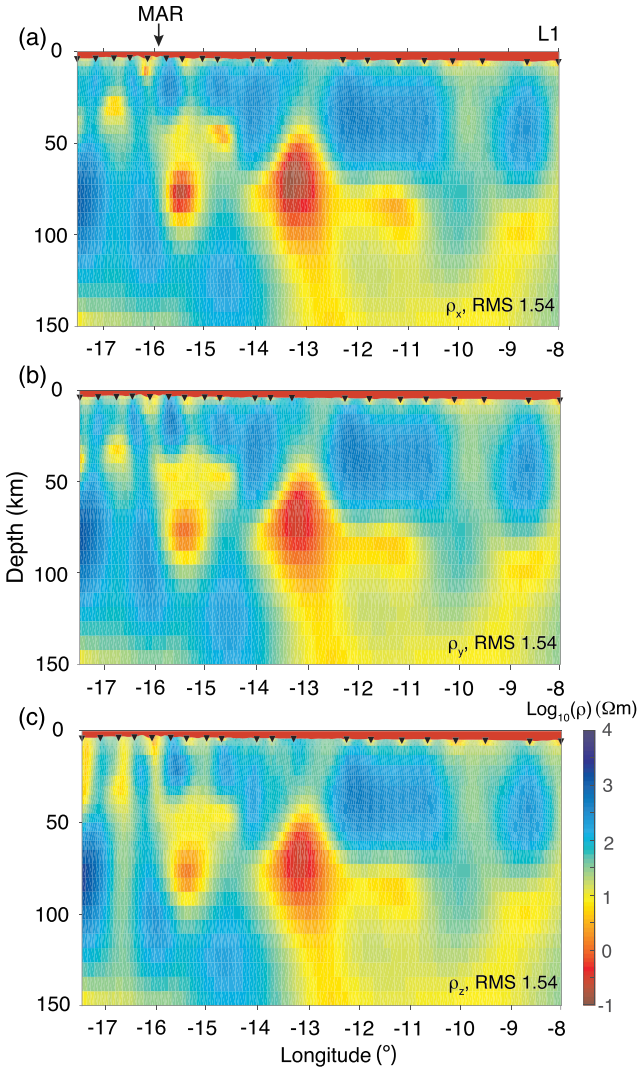

Figure 5. Resistivity models of Profile L1 (a) along *x* direction (approximately parallel to the ridge), (b) along *y* direction (approximately perpendicular to the ridge), and (c) along *z* direction. The results are very similar to the isotropic inversion (Figure 4a). Data fits are shown in Figure 7a.

step, the inversion mainly reduces model roughness starting from the best model in the first step. The inversion of the data for Profiles L1 and L2 show good fits between the model and the data (Figure 3). We also tried inversions with other starting models and regularizations (1 and 100 Ωm half-space, three times higher weight on horizontal direction), and they resolved similar resistivity models, and so we conclude that the general features resolved in the inversions are robust.

The inversion model along L1 has a RMS of 1.65 with a 10% error floor. At a broad scale, we observe a resistive lid (>100 Ohm m) that ranges in thickness between 20 to 80 km at shallow depths. At greater depths the resistivity is lower, and there are several discrete conductive patches (<1 Ohm m), which we have labeled b and c (Figure 4a). The MAR along L1 is at −16°W and corresponds to a conductive feature.

The inversion model along L2 has RMS of 1.85 with a 10% error floor. At 100–150 km depth, two conductive zones are resolved (g and h), although the details of the shape of them have low reliability since MT data lose resolution at these depths. The mostly interesting feature in the resistivity model is a conductive thin channel-like layer marked by a dashed line (Figure 4b), which is a very different feature compared to the two conductors at 100–150 km depth and also Anomalies b and c along the L1. We also highlight Anomalies e and d, which are resistive anomalies at ~75 km depth.

4.2. Anisotropic Inversion

Anisotropic inversions were used to examine any the electrical resistivity anisotropy. Inversion parameters are the same as for the isotropic inversions except for the number of elements (16,186 for L1 and 16,295 for L2). Similar to the observation of Key et al. (2013) at the East Pacific Rise, anisotropy along both profiles is not required (Figures 5 and 6). Even though the models used in the anisotropic inversions are about two times coarser than the ones in the isotropic inversions (due to a higher memory demand), the difference between the isotropic and anisotropic models (Figures 4–6) and misfits (Figures 3 and 7) is slight, except for a subtle indication that the material is slightly more conductive along the ridge direction (*x* direction). Therefore, the anisotropy is not further considered in the study.

4.3. Robustness of the Isotropic Inversion

The skin depth defined by Huang (2005) shows that the signals at the longest period are deeper than 150 km at all stations. Although we have achieved a good fit to the data, we examine the robustness of our anomalies that may be caused by gaps in data coverage at some parts of the profiles and the nonuniqueness of inversions (Menke, 1989; Ren & Kalscheuer, 2019).

Sensitivity analyses, including sensitivity matrices and model perturbation tests, are useful methods to determine how reliable inverted models are for certain features. The sensitivity matrix method of Schwalenberg et al. (2002) was used to show which parts of the inverted models are sensitive to the MT data. This type of sensitivity check helps to determine where the model is a result of the regularization and where there is intrinsic sensitivity. The color codes represent normalized sensitivity by the size of the respective grid elements and maximum sensitivity. The conductive Anomalies b, c, and f and the thin conductive layer show warm color indicating that they have high sensitivities from the data (Figure 8), especially the thin conductive layer along Profile L2. Resistive Anomaly d has low sensitivity (near blue color), but resistive Anomaly e has a relatively high sensitivity (near greenish color) even though it is not a conductor (Figure 8). This is surprising, as MT sensitivity is highest in conductive zones. We perturbed the resistivities of the regions marked

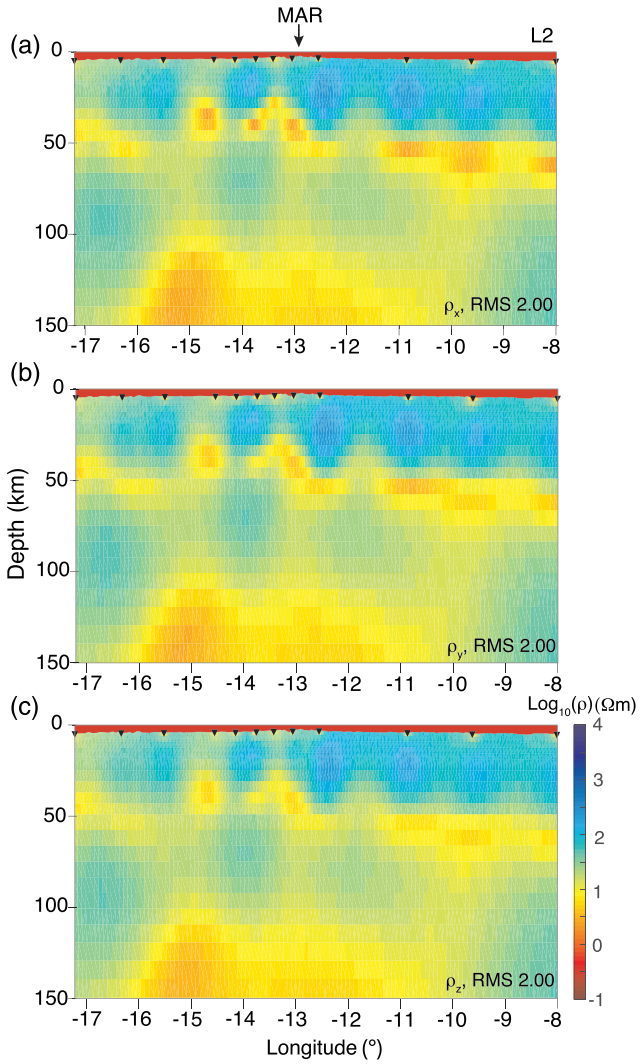

Figure 6. Resistivity models of Profile L2 (a) along *x* direction (approximately parallel to the ridge), (b) along *y* direction (approximately perpendicular to the ridge), and (c) along *z* direction. The results are very similar to the isotropic inversion too (Figure 4b). Data fits are shown in Figure 7b.

with black or white dashed lines in the inverted models (Figure 8) to 10 times higher and then compared RMS increases using forward modeling. If RMS increase due to the perturbation of a model region is high, the sensitivity of the data to this model region is high. The ratio of RMS increases corresponding to Anomalies b, c and f are about 70%, 40%, and 30%, respectively, and larger than 200% for the channel. However, the RMS increases corresponding to Anomalies e and g are only about 9% and 2%, respectively. Thus, resistive Anomaly e has only high sensitivities to not be conductor and the conductors (g and h) deeper than 100 km are poorly constrained.

We also did synthetic model tests. The main anomalies in Profiles L1 and L2 are used to generate two synthetic models (Figures 9a and 9b). The field configuration, such as station spacing and frequency, is used to calculate the forward responses, and 10% Gaussian noise is added in the synthetic data set to simulate the field data. The contaminated data were used to run inversions and test, which features can be recovered by the determinant inversion. The inversion parameters for L1 and L2 are the same as the ones used in Figure 4, accordingly. The misfit of L2 is lower than for L1 (Figure 10) due to the complexity of L1. Based on the synthetic tests, Anomalies b and c along L1 and Anomalies e and f and the thin layer along L2 can be recovered by the data set (Figures 9c and 9d). Anomalies g and h are poorly constrained. However, the undulation of the lithosphere thickness appears in the resistivity model and could be artifacts due to the lack of lateral resolution at large MT station spacing (Figures 9b and 9d). The conductors at shallow depth associated with data at −11°W to −8°W along L2 may also be a result of station spacing (Figures 4b); anisotropic inversion also indicates this (Figures 4b and 6b).

4.4. Modeling of Effects of Partial Melts on Resistivity

The conductive patches in the resistivity models are probably caused by partial melts. Resistivity of rocks decreases when charge transport is possible through an interconnected melt film coating the grains (Nover, 2005). In the suboceanic asthenosphere, estimates from MT and geomagnetic induction studies suggest partial melt content can range from approximately 0.45% to 9% (Drury, 1978). Also, geochemical study of basaltic glasses in the equatorial portion of the MAR between 3°S and 5°N showed that low-degree melting of the "transform fault effect" samples can be average of 7%, and 10% maximally (Le Voyer et al., 2015).

Two key parameters that determine the onset of dehydration partial melting are the temperature relative to the dry solidus and the concentration of H_2O in the incipient melt (Hirschmann et al., 2009). H_2O has the potential to lower the peridotite solidus and stabilize partial melts at typical mantle temperature and great depths (Novella & Frost, 2014). Although CO_2 plays a role in reducing the partial melt proportion required to maintain a high conductivity (Hirschmann, 2010), the low partial melt fraction (0.1–0.5%) maintained by CO_2 melting is far less than observed in geophysical and other experiments, which is typically about one to a few percent (Drury, 1978; Le Voyer et al., 2015; Naif et al., 2013; Ni et al., 2011; Workman & Hart, 2005). Additionally, the effect of small amounts of CO_2 on the order of 0.5 wt% on electrical conductivity is small compared to the effect of H_2O (Ni et al., 2011). Therefore, only H_2O is considered in this study.

The geophysically and petrophysically interesting temperatures of 1,300°C, 1,350°C, and 1,400°C are used for melt resistivity in Figure 11 (Constable, 2006; Ni et al., 2011). Mid-ocean ridge basalt (MORB) is typically considered to contain 50–200 ppm H_2O from early studies (Salters & Stracke, 2004). Estimates for H_2O in the

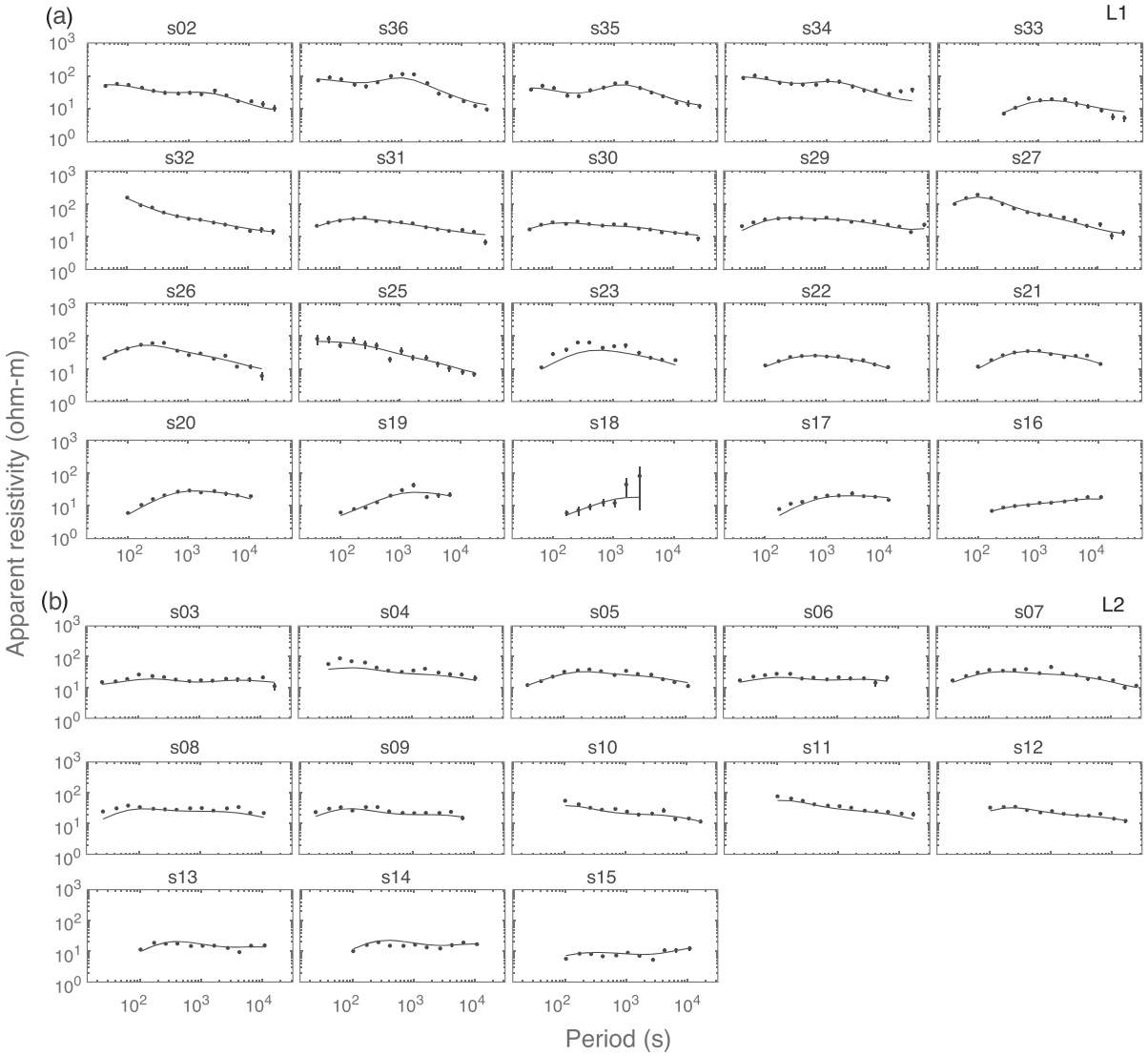

Figure 7. Observed MT data (black dots) are compared to the MT responses of the anisotropic resistivity models in Figures 5 and 6 (black lines). (a) Fits along L1. The RMS of the inversion is 1.54 with respect to a 10% error floor. (b) Fits along L2. The RMS of the inversion is 2.00 with respect to a 10% error floor. Small error bars are covered by the data dots.

mantle source for erupted lavas from 3°N to 2°S at the equatorial MAR, that is our study area, are slightly elevated from this, 110–750 ppm, with water contents of the parental magmas of 689–7,697 ppm (Le Voyer et al., 2015). Similarly, high H_2O contents in the olivine from basalts and picrites from the North Atlantic Volcanic Province indicate melting of mantle material containing >300 ppm H_2O (Jamtveit et al., 2001). In other ocean basins, such as the Pacific, a high water content of 275 ppm is needed to sustain partial melt observed offshore of Nicaragua (Naif et al., 2013). The ability of MT to resolve differences in resistivity due to increasing water content greater than 500 ppm water in basaltic melts is subtle and more tenuous as Ni et al. (2011) found from studying electrical resistivity of hydrous basalt melts at 2 GPa with 0.02 to 6.3 wt% H_2O (Figure 11a).

Overall, with 110–500 ppm H_2O in the mantle, it is likely partial melt exists in the mantle beneath our study region at depths near the solidus. The resistivity of MORB at 2GPa (Figure 11a) is calculated based on the temperature and H_2O content dependence of melt resistivity. The highest resistivity variation is limited to about 1 log unit, and stronger variation is expected at colder temperature (Figure 11a), which is consistent with Gardés et al. (2014). The estimated melt resistivity taken together with an average value of 0.006 for

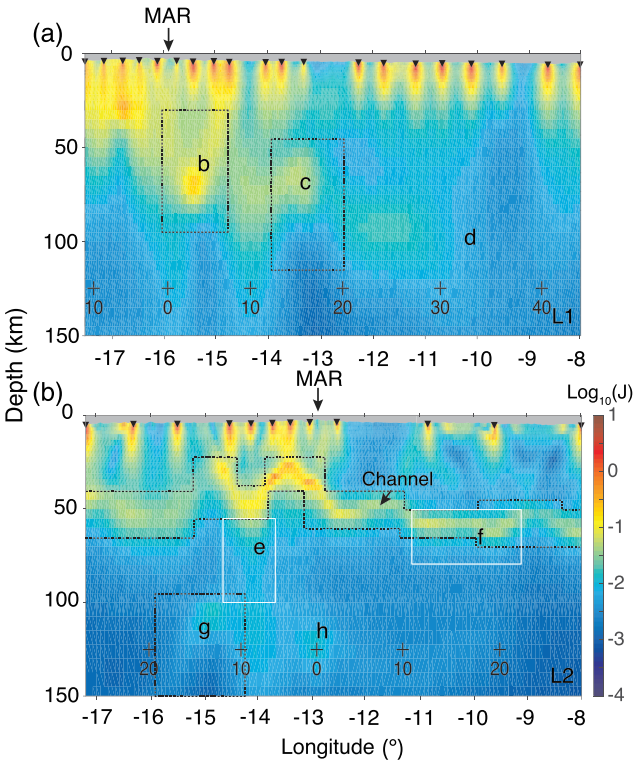

Figure 8. Sensitivity calculated for the models in Figure 4. (a) Along Profile L1 and (b) along Profile L2. The total sensitivities were computed as sums over all data points of the sensitivities normalized by data deviation and cell area following Schwalenberg et al. (2002). Anomalies b, c, e, and d and the thin conductive layer have high sensitivities from the observations. Triangles represent MT instruments. Dashed lines mark the selected regions for model perturbation test.

the water partition coefficient between solidus mantle and melt (Hirschmann et al., 2009; Ni et al., 2011) is used to calculate the resistivity of a partially molten mantle. The theory used is the Hashin and Shtrikman (1962) upper bound (HS+), and the solid mantle resistivity used is 100 Ωm (Yoshino et al., 2006). The calculated resistivities show a good match with our resistivity anomalies, such as b and c along Profile L1 and f and the conductive channel along Profile L2, when the melt fraction is about 1–7% (Figure 11b). This melt estimate is compatible with 1.5–4.5% melt fraction beneath the Atlantic lithosphere from geomagnetic induction and MT study (Drury, 1978), 1–2% melt fraction at the East Pacific Rise and the offshore of Nicaragua from MT studies (Evans et al., 1999; Naif et al., 2013), 0.25–1.25% melt fraction for the shear wave velocity reduction at oceanic LAB (Kawakatsu et al., 2009), and up to 2% of hydrous basaltic melt from petrophysical experiments (Hirth & Kohlstedt, 1996; Ni et al., 2011).

The upper limits of our estimates are within the range of the total amount of melt predicted to be extracted from the mantle to generate the oceanic crust at the surface and could be consistent with our observation if that amount of melt is generated and coalesces in the mantle near our anomalies. For instance, 6% melt fraction is needed to explain depleted MORB geochemistry in general (Workman & Hart, 2005), and an average of 7–10% partial melt of the upper mantle is needed in the equatorial portion of the MAR, for example, our study region between 3°S and 5°N to explain the MORB geochemistry (Le Voyer et al., 2015). Salters and Stracke (2004) reported average MORB composition can be explained by ~8–10% melt of the upper mantle, which is also compatible with our estimates at 1,300°C (Figure 11b). Although Anomaly c (Figure 4a) shows a lower resistivity than 1 Ωm, it can be interpreted as concentrated melts, since the mantle melt can reach a resistivity of 0.1 Ωm at relevant temperature, pressure, and water content (Figure 11a). Anomaly c may indicate that melt remains in its source area until a "critical melt fraction," such as >10% (Ni et al., 2011; Yoshino et al., 2012), is reached, whereupon the melt will segregate and ascend (Glover et al., 2000).

5. Discussions

5.1. Results Evaluation

Uncertainty in the inversions was qualitatively evaluated by testing inversions with different parameters, skin depth analysis (Huang, 2005), sensitivity analysis (Ren & Kalscheuer, 2019; Wang, Bastani, Constable, et al., 2019), model perturbation tests (Key et al., 2013), and synthetic tests (Wang, Bastani, Constable, et al., 2019). Those steps provide confidence that the anomalies in the resistivity models are robust and reliable. The inverted models passed the evaluation of inversion parameter tests and skin depth. Sensitivities lower than 65% confidence (Jacobian percentiles) are masked as gray region in the models (Figure 4). The synthetic tests as well as the model perturbation tests show that Anomalies b, c, and f and the channel can potentially be resolved by the observed marine MT data. Other anomalies have relatively low reliability, especially for g and h.

Surface-wave tomography and receiver function analysis were also used to support the MT resistivity models of the LAB at the MAR (Harmon et al., 2020; Rychert et al., 2019; Wang, Constable, Rychert, & Harmon, 2019). Conductors c and f are located in a low surface-wave velocity zone (<4.15 km/s shear velocity). Resistor d is located in a high surface-wave velocity zone. The negative phase imaged by the receiver functions, caused by a velocity decrease with depth consistent with the LAB, shows a reasonable match with the top of Conductors b and c and the top of the conductive channel. The LAB is not visible everywhere in

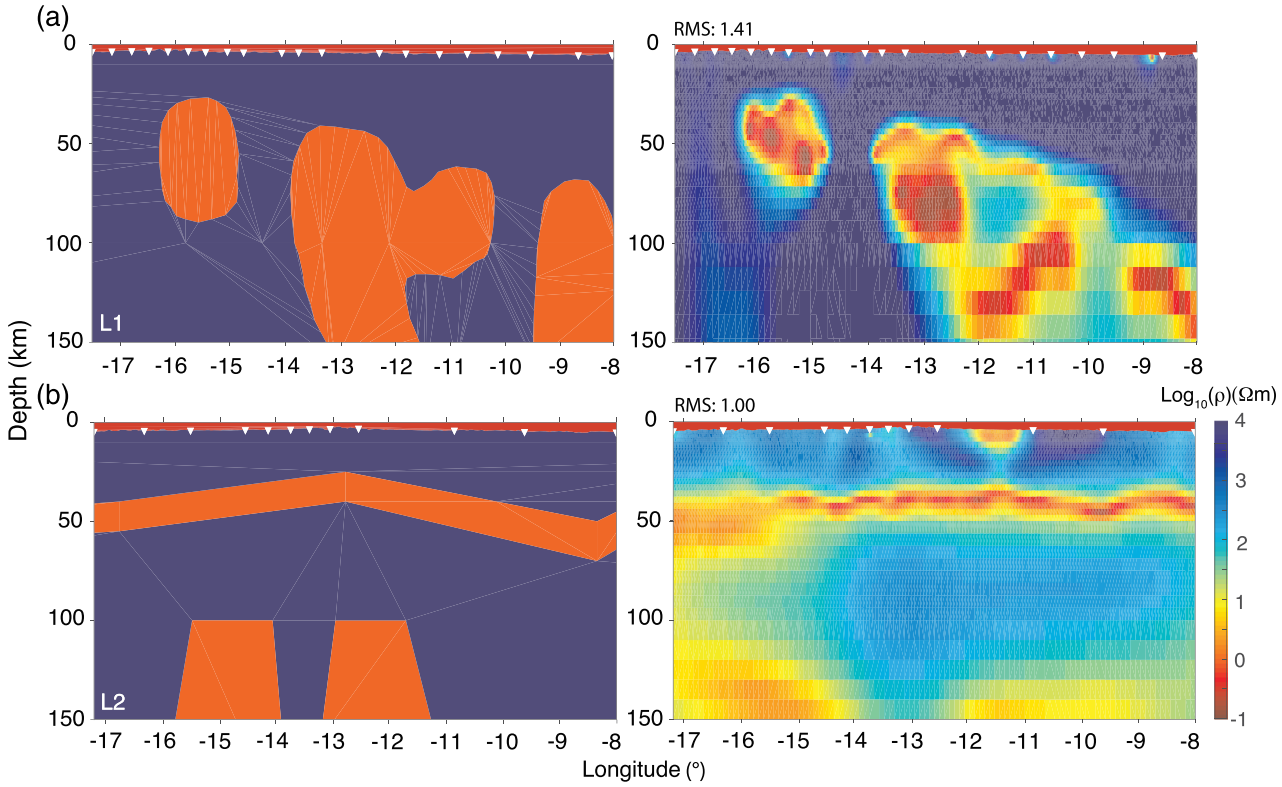

Figure 9. Structural recovery tests. (a) Synthetic model for L1, (b) synthetic model for L2, (c) recovered model for (a), and (d) recovered model for (b). Field data settings are used in the synthetic tests. The general features of the synthetic models are recovered. Data fits are shown in Figure 10.

the study region from different data analyses, for example, the distance of −10° (in the location of Anomaly d) along L1 (Figure 4), which indicates that the LAB may vary laterally in character, rather than being a sharp, singular geophysical feature.

5.2. The Partial Melt Hypothesis

Results from various laboratories are in some disagreement with regards to subsolidus mantle resistivity. Both the number and mobility of charges carriers increase with temperature, which makes electrical conductivity thermally activated in the mantle. Connectivity of the grain boundaries may be important for dry olivine (Constable, 2006; Pommier et al., 2018). It has been proposed that hydrogen within the olivine crystal lattice could cause the conductive features observed in the asthenosphere (Karato, 1990). However, careful reanalysis of all available laboratory data and the hydrogen content of the olivine samples suggest only a moderate effect (1 log unit) on conductivity at temperatures and pressures of the upper asthenosphere (Gardés et al., 2014). While debate is ongoing about the contribution of water to subsolidus conductivity in olivine, near the melting point its role is mainly to lower the melting point and increase the melt conductivity of the resulting melt. Graphite and sulphides can also enhance conductivity if highly connected, but this is unlikely to explain the low resistivity observed over great distance here (<1 Ωm). Experimentally measured resistivity for strained olivine has also shown conductive features (Pommier et al., 2018), but the measured resistivities, >10 Ωm, are too high to explain the resistivities inverted from our MT data. Previous geophysical observations (Evans et al., 2005; Key et al., 2013; Naif et al., 2013) may be explained by partial melt rather than the hydration of olivine, since a depth of 250 km with 200 ppm H_2O, or a hydrogen concentration exceeding the maximum solubility of H_2O in olivine at 3 GPa, is required to explain the resistivity of 10 Ωm (Gardés et al., 2014; Yoshino et al., 2006). Thus, the partial melt is a preferred hypothesis to interpret the conductive anomalies observed at the MAR along the profiles.

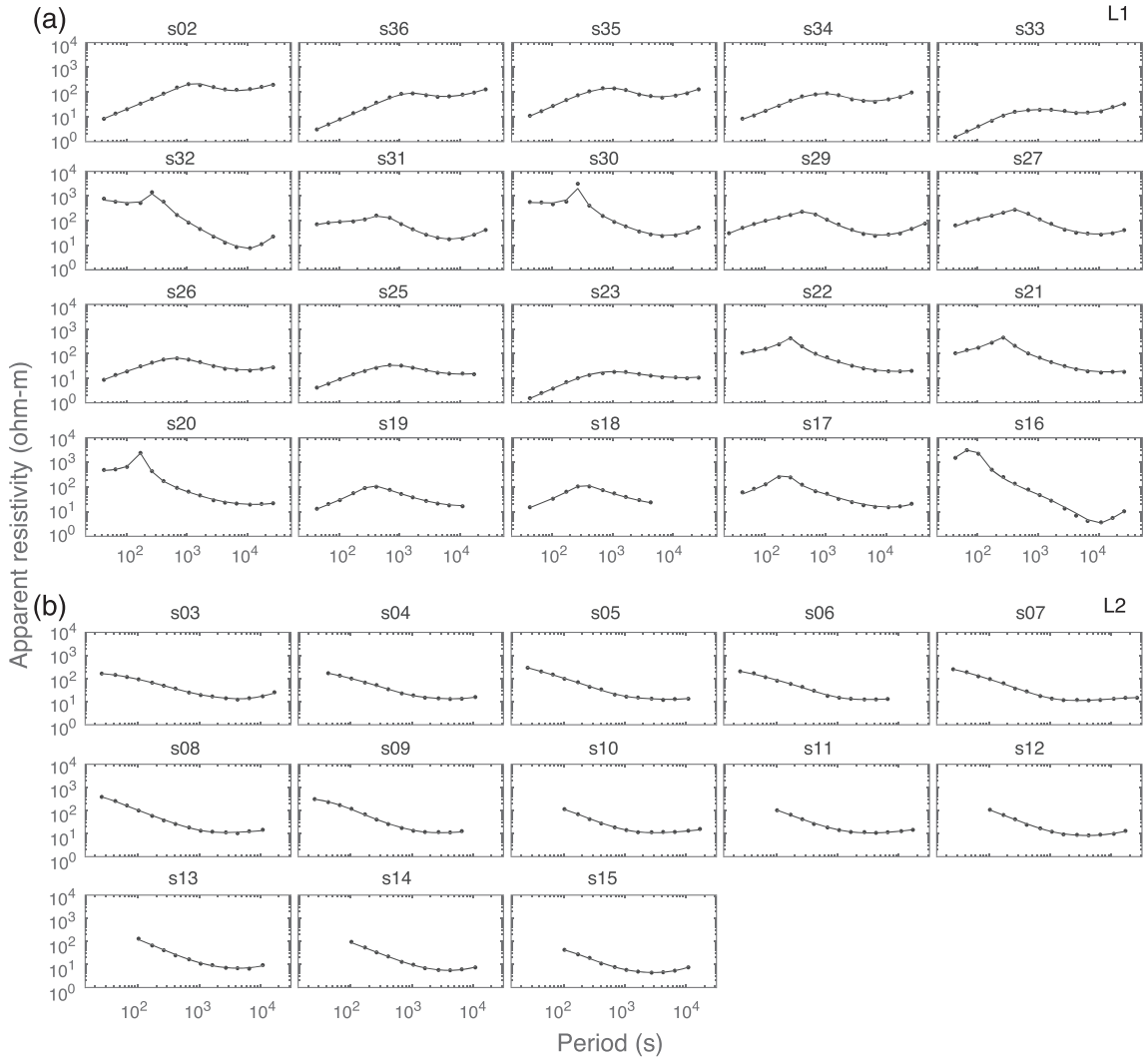

Figure 10. Simulated MT field data (black dots) are compared to the MT responses of the preferred resistivity models in Figure 9 (black lines). (a) Fits along L1. The RMS of the inversion is 1.41 with respect to a 10% error floor. (b) Fits along L2. The RMS of the inversion is 1.00 with respect to a 10% error floor. Error bars are covered by the data dots.

Partial melt increases conductivity by an order of magnitude in hydrated mantle (Ni et al., 2011), and conductivity is dominated by melt fraction. Thus, the melt fraction is the most important property of two-phase conducting materials, such as melt and (sub)solidus mantle. The resistivity of partially molten mantle estimated with HS+ model is compatible with the observations of MT data at the melt fraction of 1–7%. The melt fraction of ~0.25% and ~1% was for normal MORB and back-arc MORB region, respectively (Karato & Jung, 1998). The melt discrepancy of normal MORB to our result can be caused by uncertainties in the measurements and different compositions applied, such as H_2O and CO_2 (Hirschmann, 2010; Yoshino et al., 2012). As discussed earlier, there is geochemical evidence that there may be higher water concentrations in the upper mantle beneath L1 in our study region (Le Voyer et al., 2015) greater than the typical mantle average 116 ppm (e.g., Salters & Stracke, 2004; Workman & Hart, 2005). These levels may facilitate partial melting both on- and off-axis and generate melt volumes in line with our estimates. The existence of partial melt is also supported by low shear velocities in the asthenosphere observed by Rayleigh wave tomography, which also likely require melt. Upper limit estimates of partial melt based on shear velocity reduction require 1.5% melt fraction (Harmon et al., 2020), in good agreement with the lower limit estimates obtained from the MT data. We note that higher water

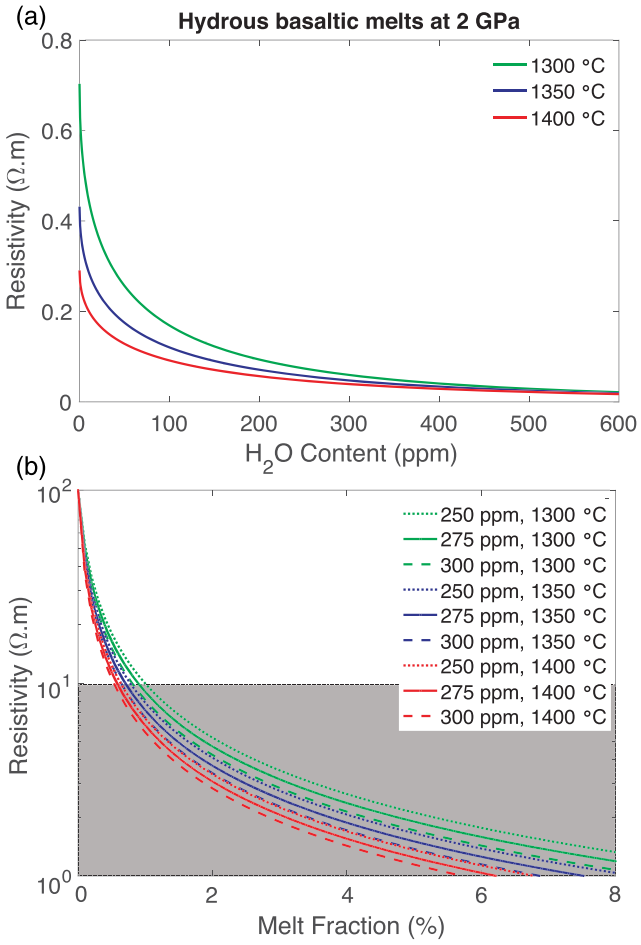

Figure 11. Relation between resistivity, water content, temperature, and partial melts. (a) Resistivity variation of hydrous basaltic melts against water content at different temperatures. (b) Resistivity variation of partially molten mantle against melt fraction at different temperatures with different water contents. Gray zone shows the resistivity values of the potential partial melts observed in the resistivity models at the MAR. The partial melt fraction can be 1–7% based on these estimations. The pressure referred is 2 GPa; at higher pressure the calculated resistivity may differ slightly based on the assumption of petrophysical conditions for the LAB.

concentrations, such as >300 ppm suggested by Le Voyer et al. (2015) and Jamtveit et al. (2001), beneath L1 require lower melt volumes to match our observations, again putting our result in good agreement with the seismic analysis. Therefore, the MT method is able to distinguish subsolidus and partially molten mantle and map the partial melt distributions, and this is particularly well done in combination with geochemical and seismic analyses.

5.3. The Dynamic LAB

The lithosphere beneath the oceans is different from the lithosphere beneath the continents (Artemieva, 2009; Eaton et al., 2009; Jones et al., 2010; Kawakatsu et al., 2009). The continents have experienced a complex geological history, and their thickness varies from about 100 to 300 km as represented by a large number of geophysical studies (Jones et al., 2010). On the other hand, the oceanic lithosphere is thinner and younger and has a simpler geological history and therefore provides a relatively clear environment in which to test competing models for the evolution of the LAB (Baba et al., 2006; Evans et al., 2005; Johansen et al., 2019; Karato, 2012; Kawakatsu et al., 2009; Key et al., 2013; Naif et al., 2013).

However, the oceanic LAB in our study is more complicated than that in classic models of the ocean lithosphere. Models in which the lithosphere-to-asthenosphere transition is primarily controlled by temperature would predict a systematic and monotonic increase in the LAB depth with plate age and distance from the ridge (Baba et al., 2006; Johansen et al., 2019; Key et al., 2013). This feature is partially delineated as a 1,200°C isotherm and partially as a 1,300°C isotherm along both profiles, especially L1 (Figure 4), but it is clearly hard to represent the LAB in our study region using a single isotherm. The nearly invariant depth of LAB in Evans et al. (2005) and Naif et al. (2013) is a result of by the relative independence of seafloor age in these studies, which is not the case in our research area, which spans 0–40 My seafloor age. In addition, a LAB that reflects only temperature would appear as a velocity drop distributed over tens of kilometers. This could be consistent with the locations where we do not observe a strong decrease in resistivity with depth (Figure 4). However, in other locations (Anomalies b, c, and f and the channel), we find relatively sharp drops in resistivity with depth, which could be explained by melt ponded along the peridotite solidus (Sparks & Parmentier, 1991). In some locations, the melt may gradually decrease with depth over tens of km (Anomaly c and west of Anomaly e). In other locations, in particular along much of L2, our anomaly suggests a thin channel of melt, similar to that interpreted by active source seismic studies beneath the Pacific Plate descending beneath New Zealand (Stern et al., 2015) and just north of our study area at the St. Paul Fracture Zone (Mehouachi & Singh, 2018). Both profiles show accumulated melts beneath the MAR, which is consistent with Sinha et al. (1997). The LAB along L1 indicates that magma may travel vertically through a ductile region at the ridge, following the low-strength, low-viscosity, and high-porosity pathway left by previous upwelling events (Keller et al., 2017). A similar feature could be observed at 100–150 km depth along L2, even though the resolution along L2 at great depth is limited. The LAB along L2 indicates that, when the upwelling magma reaches the base of the lithosphere, the magma interacts with extensional tectonic stresses and percolates along-axis through the brittle layer laterally as a ponding channel. This can be inferred as one form of partial melts (Hirschmann, 2010) and has been indicated with seismic data at the LAB (Grevemeyer, 2020; Kawakatsu et al., 2009; Magde et al., 2000) and is also consistent with the geodynamic modeling (Keller et al., 2017; Sim et al., 2020). In either case, a permeability

barrier due to high viscosity at the lithosphere base is inferred to trap buoyant melt beneath, rather than allowing it to percolate to shallower depths (Naif et al., 2013). Obviously, high water contents are necessary to lower viscosity for dynamic upwelling as suggested (Karato & Jung, 1998). In order to maintain the ponding of partial melt, hotter upwelling magma at deeper depth must be continuously or intermittently resupplied by percolation. Clearly, the LAB at the MAR is complex and can only be represented by a dynamic model.

6. Conclusions

As an aseismic boundary, the LAB at the central Middle Atlantic Ridge (MAR) was studied along a 0–45 My age range by using the marine MT method with 2-D determinant inversion. The 2-D determinant inversion is useful when 3-D distortions are not serious; otherwise, a 3-D inversion with bathymetry inclusion would be necessary. Marine MT data have sensitivity to resolve the depth of the LAB increasing with age, and the distribution of the potential partial melts near the LAB at the MAR is mapped in resistivity models. The potential partial melts used to define the LAB along the two profiles show different features. The one along Profile L1, north of the CFZ, shows a patch-like upwelling of melts near the ridge. The one along Profile L2, south of the CFZ, shows a partially melted channel most likely fed by deeper melts. A simple LAB is not resolved in all sections of Profile L1 with MT, but the patchy and potentially undulating character of the LAB above our asthenospheric anomalies is consistent with similar features in other geophysical studies in the region. Clearly, a dynamic model of the LAB is suggested by this study. The partial melt fraction calculated from the resistivity model with the support of petrophysical studies shows that 1–7% melts are needed in the hydrous basalts to maintain the resistivity values obtained in the MT inversions. This is compatible with other studies. The new understanding of the LAB from MT result supports the dynamics of plate tectonics. The observed resistivity from MT result at the central MAR provides more information to compare with the petrophysical experiments for a better understanding of the slow spreading ocean ridge.

Data Availability Statement

MT data that were used in this study can be download online (at https://marineemlab.ucsd.edu/Projects/iLAB/index.html). The raw time series have been uploaded to the Marine Geoscience Data System as per NSF policy (the doi is 10.1594/IEDA/324727). The modified MARE2DEM is available to anyone under the condition of acknowledging the contributions of Kerry Key to develop the original MARE2DEM. S.C. directed the MT experiment.

Acknowledgments

We thank the captain and crew of the R/V Marcus Langseth and the RRS Discovery, the scientific technicians, and Dan Bassett who represented the MT group on the deployment cruise. S. C. was funded by the National Science Foundation under Grant OCE-1536400 (CA-LAB). S. W. was funded by the Cecil and Ida Green Foundation and the Seafloor Electromagnetic Methods Consortium at Scripps Institution of Oceanography. C. A. R. and N. H. were funded by the Natural Environment Research Council (NE/M003507/1) and the European Research Council (GA 638665). The editor Maureen Long, Benjamin S. Murphy, and another anonymous reviewer are appreciated for constructive comments. Mingming Li and Shi J. Sim are appreciated for thoughtful discussions. Valeria Reyes-Ortega is thanked for contributions to the data preparation.

References

Agius, M. R., Harmon, N., Rychert, C. A., Tharimena, S., & Kendall, J.-M. (2018). Sediment characterization at the equatorial Mid-Atlantic Ridge from *P*-to-*S* teleseismic phase conversions recorded on the PI-LAB experiment. *Geophysical Research Letters*, *45*, 12,244–12,252. https://doi.org/10.1029/2018GL080565

Artemieva, I. M. (2009). The continental lithosphere: Reconciling thermal, seismic, and petrologic data. *Lithos*, *109*(1–2), 23–46. https://doi.org/10.1016/j.lithos.2008.09.015

Baba, K., Chave, A. D., Evans, R. L., Hirth, G., & Mackie, R. L. (2006). Mantle dynamics beneath the East Pacific Rise at 17°S: Insights from the Mantle Electromagnetic and Tomography (MELT) experiment. *Journal of Geophysical Research*, *111*, B02101. https://doi.org/10.1029/2004JB003598

Baba, K., Chen, J., Sommer, M., Utada, H., Geissler, W. H., Jokat, W., & Jegen, M. (2017). Marine magnetotellurics imaged no distinct plume beneath the Tristan da Cunha hotspot in the southern Atlantic Ocean. *Tectonophysics*, *716*, 52–63. https://doi.org/10.1016/j.tecto.2016.09.033

Baba, K., Tada, N., Matsuno, T., Liang, P., Li, R., Zhang, L., et al. (2017). Electrical conductivity of old oceanic mantle in the northwestern Pacific I: 1-D profiles suggesting differences in thermal structure not predictable from a plate cooling model. *Earth, Planets and Space*, *69*(1), 111. https://doi.org/10.1186/s40623-017-0697-0

Berdichevsky, M. N., Vanyan, L. L., Kuznetsov, V. A., Levadny, V. T., Mandelbaum, M. M., Nechaeva, G. P., et al. (1980). Geoelectrical model of the Baikal region. *Physics of the Earth and Planetary Interiors*, *22*(1), 1–11. https://doi.org/10.1016/0031-9201(80)90095-3

Burgos, G., Montagner, J.-P., Beucler, E., Capdeville, Y., Mocquet, A., & Drilleau, M. (2014). Oceanic lithosphere-asthenosphere boundary from surface wave dispersion data. *Journal of Geophysical Research: Solid Earth*, *119*, 1079–1093. https://doi.org/10.1002/2013JB010528

Constable, S. (2006). SEO3: A new model of olivine electrical conductivity. *Geophysical Journal International*, *166*(1), 435–437. https://doi.org/10.1111/j.1365-246X.2006.03041.x

Constable, S., Key, K., & Lewis, L. (2009). Mapping offshore sedimentary structure using electromagnetic methods and terrain effects in marine magnetotelluric data. *Geophysical Journal International*, *176*(2), 431–442. https://doi.org/10.1111/j.1365-246X.2008.03975.x

Cox, C., Teramoto, T., & Filloux, J. (1964). On coherent electric and magnetic fluctuations in the sea. In *Studies on Oceanography* (pp. 449–457). Tokyo. https://doi.org/10.1016/0011-7471(65)90881-8

Drury, M. J. (1978). Partial melt in the asthenosphere: Evidence from electrical conductivity data. *Physics of the Earth and Planetary Interiors*, *17*(2), P16–P20. https://doi.org/10.1016/0031-9201(78)90045-6

Eaton, D. W., Darbyshire, F., Evans, R. L., Grütter, H., Jones, A. G., & Yuan, X. (2009). The elusive lithosphere-asthenosphere boundary (LAB) beneath cratons. *Lithos*, *109*(1–2), 1–22. https://doi.org/10.1016/j.lithos.2008.05.009

Egbert, G. D. (1997). Robust multiple-station magnetotelluric data processing. *Geophysical Journal International*, *130*(2), 475–496. https://doi.org/10.1111/j.1365-246X.1997.tb05663.x

Evans, R. L., Hirth, G., Baba, K., Forsyth, D., Chave, A., & Mackie, R. (2005). Geophysical evidence from the MELT area for compositional controls on oceanic plates. *Nature*, *437*(7056), 249–252. https://doi.org/10.1038/nature04014

Evans, R. L., Tarits, P., Chave, A. D., White, A., Heinson, G., Filloux, J. H., et al. (1999). Asymmetric electrical structure in the mantle beneath the East Pacific Rise at 17°S. *Science*, *286*(5440), 752–756. https://doi.org/10.1126/science.286.5440.752

Filloux, J. H. (1980). Magnetotelluric soundings over the northeast Pacific may reveal spatial dependence of depth and conductance of the asthenosphere. *Earth and Planetary Science Letters*, *46*(2), 244–252. https://doi.org/10.1016/0012-821X(80)90010-2

Gaherty, J. B., & Jordan, T. H. (1995). Lehmann discontinuity as the base of an anisotropic layer beneath continents. *Science*, *268*(5216), 1468–1471. https://doi.org/10.1126/science.268.5216.1468

Gardés, E., Gaillard, F., & Tarits, P. (2014). Toward a unified hydrous olivine electrical conductivity law. *Geochemistry, Geophysics, Geosystems*, *15*, 4984–5000. https://doi.org/10.1002/2014GC005496

Glover, P. W. J., Pous, J., Queralt, P., Muñoz, J.-A., Liesa, M., & Hole, M. J. (2000). Integrated two-dimensional lithospheric conductivity modelling in the pyrenees using field-scale and laboratory measurements. *Earth and Planetary Science Letters*, *178*(1–2), 59–72. https://doi.org/10.1016/S0012-821X(00)00066-2

Grevemeyer, I. (2020). Upper mantle structure beneath the Mid-Atlantic Ridge from regional waveform modeling. *Bulletin of the Seismological Society of America*, *110*(1), 18–25. https://doi.org/10.1785/0120190080

Harmon, N., Rychert, C., Agius, M., Tharimena, S., Bas, T. L., Kendall, J. M., & Constable, S. (2018). Marine geophysical investigation of the chain fracture zone in the equatorial Atlantic from the PI-LAB experiment. *Journal of Geophysical Research: Solid Earth*, *123*, 11,016–11,030. https://doi.org/10.1029/2018JB015982

Harmon, N., Rychert, C., Kendall, J. M., Agius, M., Bogiatzis, P., & Tharimena, S. (2020). Evolution of the oceanic lithosphere in the equatorial Atlantic, evidence for small-scale convection from the PI-LAB experiment. *Geochemistry, Geophysics, Geosystems*, *21*, e2020GC009174. https://doi.org/10.1029/2020GC009174

Hashin, Z., & Shtrikman, S. (1962). A variational approach to the theory of the effective magnetic permeability of multiphase materials. *Journal of Applied Physics*, *33*(10), 3125–3131. https://doi.org/10.1063/1.1728579

Heinson, G., & Constable, S. (1992). The electrical conductivity of the oceanic upper mantle. *Geophysical Journal International*, *110*(1), 159–179. https://doi.org/10.1111/j.1365-246X.1992.tb00719.x

Hirschmann, M. M. (2010). Partial melt in the oceanic low velocity zone. *Physics of the Earth and Planetary Interiors*, *179*(1–2), 60–71. https://doi.org/10.1016/j.pepi.2009.12.003

Hirschmann, M. M., Tenner, T., Aubaud, C., & Withers, A. C. (2009). Dehydration melting of nominally anhydrous mantle: The primacy of partitioning. *Physics of the Earth and Planetary Interiors*, *176*(1–2), 54–68. https://doi.org/10.1016/j.pepi.2009.04.001

Hirth, G., & Kohlstedt, D. L. (1995). Experimental constraints on the dynamics of the partially molten upper mantle: Deformation in the diffusion creep regime. *Journal of Geophysical Research*, *100*(B2), 1981–2001. https://doi.org/10.1029/94JB02128

Hirth, G., & Kohlstedt, D. L. (1996). Water in the oceanic upper mantle: Implications for rheology, melt extraction and the evolution of the lithosphere. *Earth and Planetary Science Letters*, *144*(1–2), 93–108. https://doi.org/10.1016/0012-821X(96)00154-9

Huang, H. (2005). Depth of investigation for small broadband electromagnetic sensors. *Geophysics*, *70*(6), G135–G142. https://doi.org/10.1190/1.2122412

Jamtveit, B., Brooker, R., Brooks, K., Larsen, L. M., & Pedersen, T. (2001). The water content of olivines from the North Atlantic Volcanic Province. *Earth and Planetary Science Letters*, *186*(3–4), 401–415. https://doi.org/10.1016/S0012-821X(01)00256-4

Johansen, S. E., Panzner, M., Mittet, R., Amundsen, H. E. F., Lim, A., Vik, E., et al. (2019). Deep electrical imaging of the ultraslow-spreading Mohns Ridge. *Nature*, *567*(7748), 379–383. https://doi.org/10.1038/s41586-019-1010-0

Jones, A. G., Plomerova, J., Korja, T., Sodoudi, F., & Spakman, W. (2010). Europe from the bottom up: A statistical examination of the central and northern European lithosphere-asthenosphere boundary from comparing seismological and electromagnetic observations. *Lithos*, *120*(1–2), 14–29. https://doi.org/10.1016/j.lithos.2010.07.013

Jordan, T. H. (1981). Continents as a chemical boundary layer. *Philosophical Transactions of the Royal Society of London. Series A, Mathematical and Physical Sciences*, *301*(1461), 359–373.

Karato, S. (1990). The role of hydrogen in the electrical conductivity of the upper mantle. *Nature*, *347*(6290), 272–273. https://doi.org/10.1038/347272a0

Karato, S.-i. (2012). On the origin of the asthenosphere. *Earth and Planetary Science Letters*, *321–322*, 95–103. https://doi.org/10.1016/j.epsl.2012.01.001

Karato, S.-i., & Jung, H. (1998). Water, partial melting and the origin of the seismic low velocity and high attenuation zone in the upper mantle. *Earth and Planetary Science Letters*, *157*(3–4), 193–207. https://doi.org/10.1016/S0012-821X(98)00034-X

Kawakatsu, H., Kumar, P., Takei, Y., Shinohara, M., Kanazawa, T., Araki, E., & Suyehiro, K. (2009). Seismic evidence for sharp lithosphere-asthenosphere boundaries of oceanic plates. *Science*, *324*(5926), 499–502. https://doi.org/10.1126/science.1169499

Keller, T., Katz, R. F., & Hirschmann, M. M. (2017). Volatiles beneath mid-ocean ridges: Deep melting, channelised transport, focusing, and metasomatism. *Earth and Planetary Science Letters*, *464*, 55–68. https://doi.org/10.1016/j.epsl.2017.02.006

Key, K. (2016). MARE2DEM: A 2-D inversion code for controlled-source electromagnetic and magnetotelluric data. *Geophysical Journal International*, *207*(1), 571–588. https://doi.org/10.1093/gji/ggw290

Key, K., & Constable, S. (2011). Coast effect distortion of marine magnetotelluric data: Insights from a pilot study offshore northeastern Japan. *Physics of the Earth and Planetary Interiors*, *184*(3–4), 194–207. https://doi.org/10.1016/j.pepi.2010.11.008

Key, K., Constable, S., Liu, L., & Pommier, A. (2013). Electrical image of passive mantle upwelling beneath the northern East Pacific Rise. *Nature*, *495*(7442), 499–502. https://doi.org/10.1038/nature11932

Le Voyer, M., Cottrell, E., Kelley, K. A., Brounce, M., & Hauri, E. H. (2015). The effect of primary versus secondary processes on the volatile content of MORB glasses: An example from the equatorial Mid-Atlantic Ridge (5°N–3°S). *Journal of Geophysical Research: Solid Earth*, *120*, 125–144. https://doi.org/10.1002/2014JB011160

Lin, P.-Y. P., Gaherty, J. B., Jin, G., Collins, J. A., Lizarralde, D., Evans, R. L., & Hirth, G. (2016). High-resolution seismic constraints on flow dynamics in the oceanic asthenosphere. *Nature*, *535*(7613), 538–541. https://doi.org/10.1038/nature18012

Lizarralde, D., Chave, A., Hirth, G., & Schultz, A. (1995). Northeastern Pacific mantle conductivity profile from long-period magnetotelluric sounding using Hawaii-to-California submarine cable data. *Journal of Geophysical Research*, *100*(B9), 17,837–17,854. https://doi.org/10.1029/95JB01244

Magde, L. S., Barclay, A. H., Toomey, D. R., Detrick, R. S., & Collins, J. A. (2000). Crustal magma plumbing within a segment of the Mid-Atlantic Ridge, 35°N. *Earth and Planetary Science Letters*, *175*(1–2), 55–67. https://doi.org/10.1016/S0012-821X(99)00281-2

Maggi, A., Debayle, E., Priestley, K., & Barruol, G. (2006). Azimuthal anisotropy of the Pacific region. *Earth and Planetary Science Letters*, *250*(1–2), 53–71. https://doi.org/10.1016/j.epsl.2006.07.010

Matsuno, T., Seama, N., Evans, R. L., Chave, A. D., Baba, K., White, A., et al. (2010). Upper mantle electrical resistivity structure beneath the central Mariana subduction system. *Geochemistry, Geophysics, Geosystems*, *11*, Q09003. https://doi.org/10.1029/2010GC003101

McKenzie, D. P. (1967). Some remarks on heat flow and gravity anomalies. *Journal of Geophysical Research* (1896–1977), *72*(24), 6261–6273. https://doi.org/10.1029/JZ072i024p06261

Mehouachi, F., & Singh, S. C. (2018). Water-rich sublithospheric melt channel in the equatorial Atlantic Ocean. *Nature Geoscience*, *11*(1), 65–69. https://doi.org/10.1038/s41561-017-0034-z

Menke, W. (1989). *Geophysical data analysis: Discrete inverse theory*. Orlando: Academic Press.

Myer, D., Constable, S., Key, K., Glinsky, M. E., & Liu, G. (2012). Marine CSEM of the Scarborough gas field, Part 1: Experimental design and data uncertainty. *Geophysics*, *77*(4), E281–E299. https://doi.org/10.1190/geo2011-0380.1

Naif, S., Key, K., Constable, S., & Evans, R. L. (2013). Melt-rich channel observed at the lithosphere-asthenosphere boundary. *Nature*, *495*(7441), 356–359. https://doi.org/10.1038/nature11939

Naif, S., Key, K., Constable, S., & Evans, R. L. (2015). Water-rich bending faults at the Middle America Trench. *Geochemistry, Geophysics, Geosystems*, *16*, 2582–2597. https://doi.org/10.1002/2015GC005927

Naif, S., Key, K., Constable, S., & Evans, R. L. (2016). Porosity and fluid budget of a water-rich megathrust revealed with electromagnetic data at the Middle America Trench. *Geochemistry, Geophysics, Geosystems*, *17*, 4495–4516. https://doi.org/10.1002/2016GC006556

Ni, H., Keppler, H., & Behrens, H. (2011). Electrical conductivity of hydrous basaltic melts: Implications for partial melting in the upper mantle. *Contributions to Mineralogy and Petrology*, *162*(3), 637–650. https://doi.org/10.1007/s00410-011-0617-4

Nolasco, R., Tarits, P., Filloux, J. H., & Chave, A. D. (1998). Magnetotelluric imaging of the Society Islands hotspot. *Journal of Geophysical Research*, *103*(B12), 30,287–30,309. https://doi.org/10.1029/98JB02129

Novella, D., & Frost, D. J. (2014). The composition of hydrous partial melts of garnet peridotite at 6 GPa: Implications for the origin of Group II kimberlites. *Journal of Petrology*, *55*(11), 2097–2124. https://doi.org/10.1093/petrology/egu051

Nover, G. (2005). Electrical properties of crustal and mantle rocks—A review of laboratory measurements and their explanation. *Surveys in Geophysics*, *26*(5), 593–651. https://doi.org/10.1007/s10712-005-1759-6

Parker, R. L., & Oldenburg, D. W. (1973). Thermal model of ocean ridges. *Nature Physical Science*, *242*(122), 137–139. https://doi.org/10.1038/physci242137a0

Parsons, B., & Sclater, J. G. (1977). An analysis of the variation of ocean floor bathymetry and heat flow with age. *Journal of Geophysical Research*, *82*(5), 803–827. https://doi.org/10.1029/JB082i005p00803

Pedersen, L. B., & Engels, M. (2005). Routine 2-D inversion of magnetotelluric data using the determinant of the impedance tensor. *Geophysics*, *70*(2), G33–G41. https://doi.org/10.1190/1.1897032

Pommier, A., Kohlstedt, D. L., Hansen, L. N., Mackwell, S., Tasaka, M., Heidelbach, F., & Leinenweber, K. (2018). Transport properties of olivine grain boundaries from electrical conductivity experiments. *Contributions to Mineralogy and Petrology*, *173*(5), 41. https://doi.org/10.1007/s00410-018-1468-z

Poudjom Djomani, Y. H., O'Reilly, S. Y., Griffin, W. L., & Morgan, P. (2001). The density structure of subcontinental lithosphere through time. *Earth and Planetary Science Letters*, *184*(3–4), 605–621. https://doi.org/10.1016/S0012-821X(00)00362-9

Ranganayaki, R. P. (1984). An interpretive analysis of magnetotelluric data. *Geophysics*, *49*(10), 1730–1748. https://doi.org/10.1190/1.1441580

Ren, Z., & Kalscheuer, T. (2019). Uncertainty and resolution analysis of 2-D and 3-D inversion models computed from geophysical electromagnetic data. *Surveys in Geophysics*, *41*(1), 47–112. https://doi.org/10.1007/s10712-019-09567-3

Rychert, C., Harmon, N., Constable, S., Kendall, J. M., Tharimena, S., Wang, S., et al. (2019). A dynamic lithosphere-asthenosphere boundary dictated by variations in melt generation and migration: Results from the PI-LAB experiment in the equatorial mid Atlantic. Presented at the AGU Fall Meeting 2019, AGU. Retrieved from https://agu-do03.confex.com/agu/fm19/meetingapp.cgi/Paper/509936

Rychert, C. A., Fischer, K. M., & Rondenay, S. (2005). A sharp lithosphere-asthenosphere boundary imaged beneath eastern North America. *Nature*, *436*(7050), 542–545. https://doi.org/10.1038/nature03904

Rychert, C. A., & Harmon, N. (2017). Constraints on the anisotropic contributions to velocity discontinuities at ~60 km depth beneath the Pacific. *Geochemistry, Geophysics, Geosystems*, *18*, 2855–2871. https://doi.org/10.1002/2017GC006850

Rychert, C. A., Harmon, N., & Tharimena, S. (2018a). Scattered wave imaging of the oceanic plate in Cascadia. *Science Advances*, *4*(2), eaao1908. https://doi.org/10.1126/sciadv.aao1908

Rychert, C. A., Harmon, N., & Tharimena, S. (2018b). Seismic imaging of the base of the ocean plates. In *Lithospheric Discontinuities* (pp. 71–87). Washington DC: American Geophysical Union (AGU). https://doi.org/10.1002/9781119249740.ch4

Rychert, C. A., Rondenay, S., & Fischer, K. M. (2007). *P*-to-*S* and *S*-to-*P* imaging of a sharp lithosphere-asthenosphere boundary beneath eastern North America. *Journal of Geophysical Research*, *112*, B08314. https://doi.org/10.1029/2006JB004619

Rychert, C. A., & Shearer, P. M. (2009). A global view of the lithosphere-asthenosphere boundary. *Science*, *324*(5926), 495–498. https://doi.org/10.1126/science.1169754

Salters, V. J. M., & Stracke, A. (2004). Composition of the depleted mantle. *Geochemistry, Geophysics, Geosystems*, *5*, Q05004. https://doi.org/10.1029/2003GC000597

Sarafian, E., Evans, R. L., Collins, J. A., Elsenbeck, J., Gaetani, G. A., Gaherty, J. B., et al. (2015). The electrical structure of the central Pacific upper mantle constrained by the NoMelt experiment. *Geochemistry, Geophysics, Geosystems*, *16*, 1115–1132. https://doi.org/10.1002/2014GC005709

Schwalenberg, K., Rath, V., & Haak, V. (2002). Sensitivity studies applied to a two-dimensional resistivity model from the Central Andes. *Geophysical Journal International*, *150*(3), 673–686. https://doi.org/10.1046/j.1365-246X.2002.01734.x

Sim, S. J., Spiegelman, M., Stegman, D. R., & Wilson, C. (2020). The influence of spreading rate and permeability on melt focusing beneath mid-ocean ridges. *Physics of the Earth and Planetary Interiors*, *304*, 106486. https://doi.org/10.1016/j.pepi.2020.106486

Sinha, M. C., Navin, D. A., MacGregor, L. M., Constable, S., Peirce, C., White, A., et al. (1997). Evidence for accumulated melt beneath the slow-spreading Mid-Atlantic Ridge. *Philosophical Transactions of the Royal Society of London. Series A: Mathematical, Physical and Engineering Sciences*, *355*(1723), 233–253. https://doi.org/10.1098/rsta.1997.0008

Sparks, D. W., & Parmentier, E. M. (1991). Melt extraction from the mantle beneath spreading centers. *Earth and Planetary Science Letters*, *105*(4), 368–377. https://doi.org/10.1016/0012-821X(91)90178-K

Stein, C. A., & Stein, S. (1992). A model for the global variation in oceanic depth and heat flow with lithospheric age. *Nature*, *359*(6391), 123–129. https://doi.org/10.1038/359123a0

Stern, T. A., Henrys, S. A., Okaya, D., Louie, J. N., Savage, M. K., Lamb, S., et al. (2015). A seismic reflection image for the base of a tectonic plate. *Nature*, *518*(7537), 85–88. https://doi.org/10.1038/nature14146

Tada, N., Tarits, P., Baba, K., Utada, H., Kasaya, T., & Suetsugu, D. (2016). Electromagnetic evidence for volatile-rich upwelling beneath the society hotspot, French Polynesia. *Geophysical Research Letters*, *43*, 12,021–12,026. https://doi.org/10.1002/2016GL071331

Tharimena, S., Rychert, C., & Harmon, N. (2017). A unified continental thickness from seismology and diamonds suggests a melt-defined plate. *Science*, *357*(6351), 580–583. https://doi.org/10.1126/science.aan0741

Wang, S., Bastani, M., Constable, S., Kalscheuer, T., & Malehmir, A. (2019). Boat-towed radio-magnetotelluric and controlled source audio-magnetotelluric study to resolve fracture zones at Äspö Hard Rock Laboratory site, Sweden. *Geophysical Journal International*, *218*(2), 1008–1031. https://doi.org/10.1093/gji/ggz162

Wang, S., Constable, S., Reyes-Ortega, V., Hormoz, J., Farquharson, C., & Avilés Esquivel, T. (2020). Two-dimensional determinant inversion of marine magnetotelluric data and a field example from the Gulf of California, Mexico. *Geophysics*. https://doi.org/10.1190/GEO2019-0735.1

Wang, S., Constable, S., Reyes-Ortega, V., & Rychert, C. A. (2019). A newly distinguished marine magnetotelluric coast effect sensitive to the lithosphere-asthenosphere boundary. *Geophysical Journal International*, *218*(2), 978–987. https://doi.org/10.1093/gji/ggz202

Wang, S., Constable, S., Rychert, C., & Harmon, N. (2019). A dynamic lithosphere-asthenosphere boundary revealed using marine magnetotelluric data. *AGU Fall Meeting Abstracts*, *43*. Retrieved from http://adsabs.harvard.edu/abs/2019AGUFM.T43F0516W

Wheelock, B., Constable, S., & Key, K. (2015). The advantages of logarithmically scaled data for electromagnetic inversion. *Geophysical Journal International*, *201*(3), 1765–1780. https://doi.org/10.1093/gji/ggv107

Workman, R. K., & Hart, S. R. (2005). Major and trace element composition of the depleted MORB mantle (DMM). *Earth and Planetary Science Letters*, *231*(1–2), 53–72. https://doi.org/10.1016/j.epsl.2004.12.005

Worzewski, T., Jegen, M., Kopp, H., Brasse, H., & Castillo, W. T. (2011). Magnetotelluric image of the fluid cycle in the Costa Rican subduction zone. *Nature Geoscience*, *4*(2), 108–111. https://doi.org/10.1038/ngeo1041

Worzewski, T., Jegen, M., & Swidinsky, A. (2012). Approximations for the 2-D coast effect on marine magnetotelluric data. *Geophysical Journal International*, *189*(1), 357–368. https://doi.org/10.1111/j.1365-246X.2012.05385.x

Yoshino, T., Matsuzaki, T., Yamashita, S., & Katsura, T. (2006). Hydrous olivine unable to account for conductivity anomaly at the top of the asthenosphere. *Nature*, *443*(7114), 973–976. https://doi.org/10.1038/nature05223

Yoshino, T., McIsaac, E., Laumonier, M., & Katsura, T. (2012). Electrical conductivity of partial molten carbonate peridotite. *Physics of the Earth and Planetary Interiors*, *194–195*, 1–9. https://doi.org/10.1016/j.pepi.2012.01.005